


RESEARCH

Open Access



CsPbBr₃/graphene nanowall artificial optoelectronic synapses for controllable perceptual learning

Runze Li^{1,2†}, Yibo Dong^{1,2†}, Fengsong Qian³, Yiyang Xie³, Xi Chen^{1,2*}, Qiming Zhang^{1,2}, Zengji Yue^{1,2*}  and Min Gu^{1,2*}

[†]Runze Li and Yibo Dong contributed equally to this work.

*Correspondence:
xichen@usst.edu.cn;
zengjiyue@usst.edu.cn;
gumin@usst.edu.cn

¹Institute of Photonic Chips, University of Shanghai for Science and Technology, Shanghai 200093, China

²Centre for Artificial-Intelligence Nanophotonics, School of Optical-Electrical and Computer Engineering, University of Shanghai for Science and Technology, Shanghai 200093, China

³Key Laboratory of Optoelectronic Technology, Ministry of Education, Beijing University of Technology, Beijing, China

Abstract

The rapid development of neuromorphic computing has stimulated extensive research interest in artificial synapses. Optoelectronic artificial synapses using laser beams as stimulus signals have the advantages of broadband, fast response, and low crosstalk. However, the optoelectronic synapses usually exhibit short memory duration due to the low lifetime of the photo-generated carriers. It greatly limits the mimicking of human perceptual learning, which is a common phenomenon in sensory interactions with the environment and practices of specific sensory tasks. Herein, a heterostructure optoelectronic synapse based on graphene nanowalls and CsPbBr₃ quantum dots was fabricated. The graphene/CsPbBr₃ heterojunction and the natural middle energy band in graphene nanowalls extend the carrier lifetime. Therefore, a long half-life period of photocurrent decay - 35.59 s has been achieved. Moreover, the long-term optoelectronic response can be controlled by the adjustment of numbers, powers, wavelengths, and frequencies of the laser pulses. Next, an artificial neural network consisting of a 28 × 28 synaptic array was established. It can be used to mimic a typical characteristic of human perceptual learning that the ability of sensory systems is enhanced through a learning experience. The learning behavior of image recognition can be tuned based on the photocurrent response control. The accuracy of image recognition keeps above 80% even under a low-frequency learning process. We also verify that less time is required to regain the lost sensory ability that has been previously learned. This approach paves the way toward high-performance intelligent devices with controllable learning of visual perception.

Introduction

In the era of data torrents, the exponential growth of electronic computing power has led to deviations from Moore's Law. During large-scale computing, the von Neumann architecture using a processing unit and a separate storage unit encounters a "storage wall" bottleneck, owing to the limitation of the transmission rate between the processing unit and the storage unit [1–4]. On the other hand, human sensory neurons conduct in-memory processing. For example, a phenomenon named perceptual learning demonstrates that the ability of sensory systems to respond to stimuli can be enhanced through

a learning experience, and less time is required to regain the lost ability that has been previously learned. It is a basic mechanism for a human to process input signals with extremely high rates and low energy consumption [5]. Consequently, the elimination of the processing-storage transmission has great potential to solve the limitations of von Neumann's architecture.

Currently, neuromorphic computing that mimics in-memory processing functions of the sensory neurons has attracted intensive research interest [6, 7]. The simulation of a synapse, which is a key component of the sensory neuron has become a breakthrough point in improving the calculation speed and reducing power consumption [8]. Conventional artificial synaptic devices are operated based on the principle of resistance changes under electrical stimulations. Transistors [9, 10], phase-change materials [11], and resistive-change materials [12, 13] have been used to realize the in-memory behaviors [14]. However, the electrical synapses have limited bandwidths due to considerable interconnection problems including delays and power losses in the process of signal transmission, and thus the neuromorphic computing speed is limited [15]. In contrast, investigations have proved that optical stimulations can considerably broaden the bandwidth and alleviate the interconnection problem [16]. The devices of artificial optoelectronic synapses provide a promising pathway for neuromorphic computing [17]. More importantly, the optoelectronic synapses can accurately simulate retinal neurons, enabling high-accuracy image detection and recognition [18]. Since 80 % of the information in the external world is transmitted to the human brain through visual perception, the artificial optoelectronic synapses exhibit a noncontact input method for the development of optical wireless communications and operations [19].

Artificial optoelectronic synapses can be divided into four types - heterojunction channel (HC)-typed synapses [20–23], oxide semiconductor-based synapses [14, 24], floating gate-based synapses [25, 26], and circuit-based synapses [27, 28]. Among them, HC-typed synapses have introduced additional laser absorbers (such as perovskites [29–31], chalcogens [32–34], and organic semiconductors [35]) to form a heterojunction with high-mobility semiconductors in the channel region, showing highly sensitive photoconductance properties [36]. Moreover, the range of the photoresponse spectrum can be easily controlled by using the absorber with an appropriate bandgap. Perovskite is one of the most promising candidate materials for HC-type optoelectronics because of its high carrier mobility [37] and tunable bandgap [38]. However, perovskite-based HC-type synapses usually exhibit a very short memory time due to the rapid recombination of the captured charges at the heterogeneous interface. The challenge to achieve a significant long-term greatly response limits the simulation of typical in-memory processing behaviors such as perceptual learning [39].

Herein, to realize perceptual learning on neuromorphic computing devices, we report HC-type optoelectronic synapses based on graphene nanowalls (GNWs) and all-inorganic extremely CsPbBr₃ perovskite quantum dots (QDs). CsPbBr₃ QDs are used as laser absorbers layers and GNWs as semiconductor transmission layers. The built-in electric field of the CsPbBr₃ QDs/GNWs heterojunction can separate the photogenerated carriers, and the natural defects in GNWs can confine the transferred carriers, thus substantially extending the carrier lifetime. Moreover, the vertical nanosheet structure of GNWs can effectively increase the contact area between graphene and CsPbBr₃ QDs

to improve the memory duration of the photocurrent. Under the stimulation of a 530 nm laser pulse, an extremely high value of the half-time period of photocurrent decay up to 35.59 s can be measured. Through the utilization of an artificial neuron network (ANN) consisting of the GNWs/CsPbBr₃ QDs synaptic array, the typical characteristics of human perceptual learning can be demonstrated.

Results

GNWs/CsPbBr₃ QDs optoelectronic synapses

A biological nervous system constitutes lots of interconnected neurons to simultaneously receive information and achieve distributed in-memory processing [40]. Figure 1a presents a schematic showing a typical synaptic structure of the neural network, which consists of basic parts - cell body, axon, and dendrite. Input signals generate action

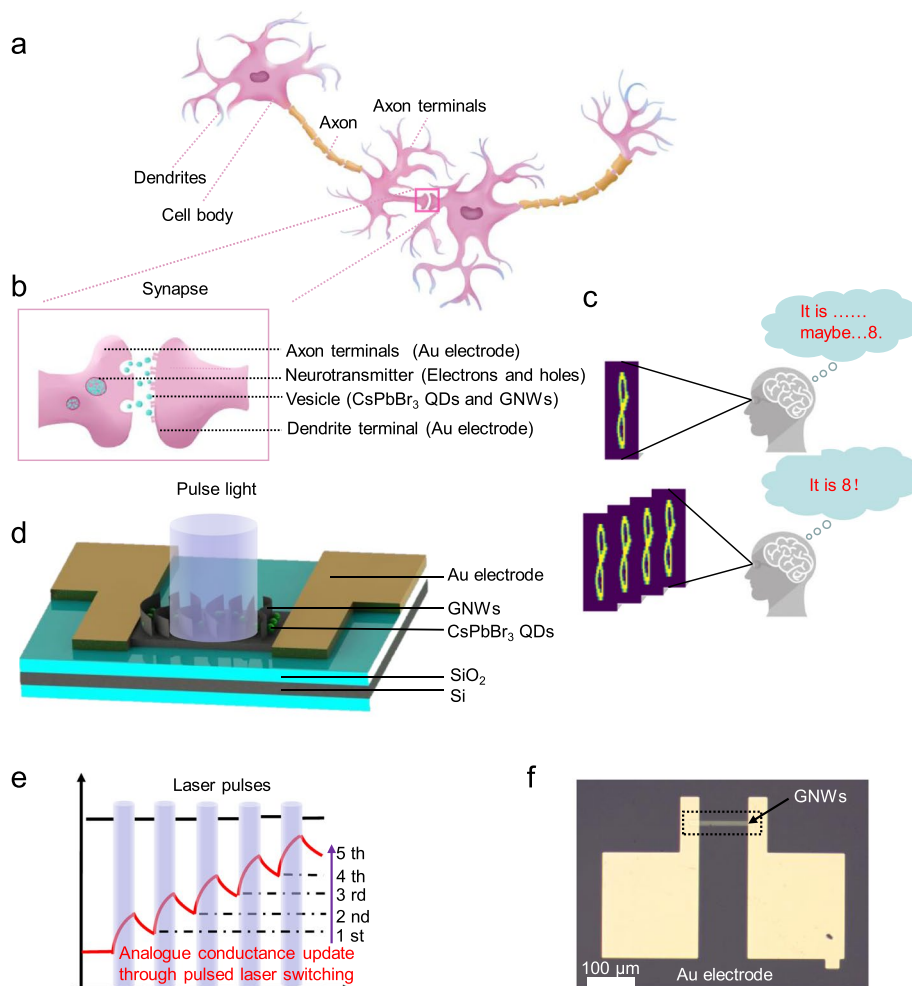


Fig. 1 A biological synaptic structure for perceptual learning and GNWs/CsPbBr₃ QDs artificial optoelectronic synapse. **a** A biological nervous system with a typical synaptic structure. **b** Schematic of a synaptic structure. **c** Schematic of human perceptual learning, in which the sensory ability can be enhanced through a learning experience. **d** Schematic of a GNWs/CsPbBr₃ QDs artificial optoelectronic synapse. **e** Schematic of photocurrent response of an artificial optoelectronic synapse generated by laser pulses. **f** An optical image of the GNWs/CsPbBr₃ QDs synapse

potentials in neurons based on stimulation, propagating through synapses for signal communication (Fig. 1b) [41]. Because of the ultra-high energy efficiency and the unique information processing mechanism, synapses conduct high-speed computing tasks with ultralow power consumption, which is almost infeasible in traditional computers. Each event of information transmission through the synaptic structure consumes only approximately 1–100 fJ [42]. The intensity of communication between neurons caused by neurotransmitters is defined as the synaptic weight, and the change in synaptic weight due to different external stimulus signals is called synaptic photoplasticity, which is considered to be the basis of brain learning and memory [43, 44].

Artificial optoelectronic synapses were fabricated to perform human perceptual learning, in which the sensory ability can be enhanced through a learning experience (Fig. 1c). The structure of the optoelectronic synapse based on GNWs and CsPbBr₃ QDs is shown in Fig. 1d, and the fabrication flowchart and the optical images of the synapse array are illuminated in Fig. S1. First, GNWs were grown on a heavily p-doped Si wafer with a SiO₂ layer using a plasma-enhanced chemical vapor deposition (PECVD) equipment. Then, the GNW array was patterned by oxygen plasma etching. Next, positive and negative electrodes were fabricated by photolithography. Finally, the CsPbBr₃ QDs were spin-coated on the GNWs. The CsPbBr₃ QDs were spin-coated on the GNWs as light absorbers. The morphologies and structures of GNWs allow CsPbBr₃ QDs to be embedded within them, thus increasing the contact area with graphene.

In the optoelectronic synapse, gold electrodes can be regarded as axon terminals and dendrite terminals, GNWs/CsPbBr₃ QDs as vesicles, and photogenerated electrons/holes of CsPbBr₃ QDs as neurotransmitters (Fig. 1b). When a pulsed laser is applied to the device, photocurrent changes can be induced (Fig. 1e). According to the optical image of the channel of the GNWs (Fig. 1f), the length and width of the GNW area are 150 μm and 14 μm, respectively. The distance between two Au electrodes is 100 μm.

Synapse characterization

Figure 2a shows a transmission electron microscopy (TEM) image of CsPbBr₃ QDs. The average diameter of the QDs is 13 nm. The detailed crystalline structures can be observed in the high-resolution transmission electron microscopy (HRTEM) image, as shown in Fig. 2b. GNWs exhibit a vertical nanosheet morphology with a sidewall height of 82 nm (Figs. 2c and S2). Through the Raman spectra of GNWs and GNWs/CsPbBr₃ QDs (Fig. 2d), a high-defect density of GNWs is shown, providing them with natural carrier-trapping characteristics [45]. Meanwhile, after doping GNWs/CsPbBr₃ QDs, the Raman shift of the G-peak changes from 1598.91 cm⁻¹ to 1592.68 cm⁻¹ due to the Kohn anomaly effect, indicating that CsPbBr₃ QDs and GNWs are n-type dopings [46, 47].

Regarding the optical properties of the CsPbBr₃ QDs, we found that their absorption peak is mainly located at 500 nm. Steady-state photoluminescence (PL) of CsPbBr₃ QDs, shown in Fig. 2e, implies that under the excitation of a 450 nm laser beam the CsPbBr₃ quantum dot film emits a sharp emission peak centered at 515 nm, which is corresponding to the absorption spectrum shown in Fig. S3. When the CsPbBr₃ QDs were coated on GNWs, the PL intensity is weakened, or even quenched, and the emission peak is shifted, which indicates an efficient photogenerated carrier

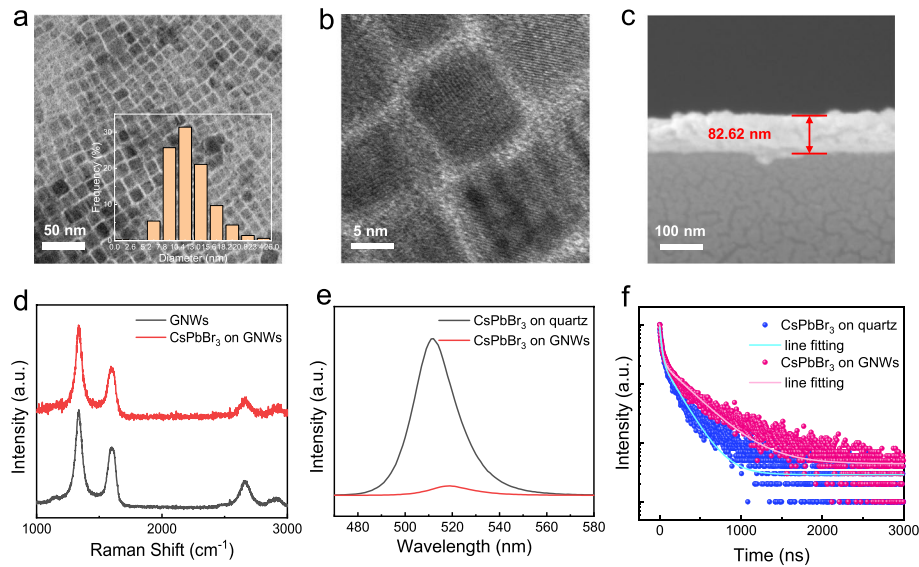


Fig. 2 Characterization of CsPbBr₃ QDs and GNWs. **a** A TEM image of CsPbBr₃ QDs on. The inset is the size distribution of QDs. **b** A HRTEM image of CsPbBr₃ QDs. **c** A side-view SEM image of the GNWs sample. **d** Raman spectra of GNWs and CsPbBr₃ QDs on GNWs. **e** PL spectra of CsPbBr₃ QDs on GNWs and a quartz substrate under 450 nm laser beam excitation. **f** PL life constant measurement of CsPbBr₃ QDs on GNWs and a quartz substrate

transfer caused by the GNWs/CsPbBr₃ QDs heterojunction. Through the GNW integration, the emission peak is red-shifted by 5 nm due to the narrowing of the bandgap of CsPbBr₃ QDs.

The PL time constant measurement of the CsPbBr₃ film and the GNWs/CsPbBr₃ QDs film was conducted under an excitation wavelength of 450 nm. The experimental results were fitted with a double exponential function to obtain the fluorescence lifetime parameters (Fig. 2f). The fitting function:

$$Y = y_0 + A_1 * e^{-\frac{x}{\tau_1}} + A_2 * e^{-\frac{x}{\tau_2}} \quad (1)$$

According to the average life expectancy calculation formula,

$$\tau_{\text{avg}} = \frac{\sum_i A_i \tau_i^2}{\sum_i A_i \tau_i} \quad (2)$$

where τ_i is the PL time constant, and A_i is the corresponding weighting factor. τ_1 and τ_2 are respectively related to nonradiative and radiative recombination [48]. The reference fitting function for the CsPbBr₃ QDs film can be extracted according to the following parameters: $\tau_1 = 21.92$ ns, $\tau_2 = 182.83$ ns, and $A_1 = 0.6503$, $A_2 = 0.2525$. The average life expectancy is 144.87 ns. On the other hand, the corresponding fitting function for the doped GNWs/CsPbBr₃ QDs film can be extracted according to the following parameters: $\tau_1 = 22.52$ ns, $\tau_2 = 323.33$ ns, and $A_1 = 0.7296$, $A_2 = 0.2340$. The average life expectancy is 269.66 ns. The results prove that the built-in electric field formed by GNWs and CsPbBr₃ QDs effectively separates the photogenerated carriers under laser beam excitation, thus reducing the recombination of photogenerated carriers in CsPbBr₃ QDs, resulting in decreasing of the fluorescence intensity and time constant, and increasing of photogenerated carrier lifetime. The extended carrier lifetime is crucial to achieving a

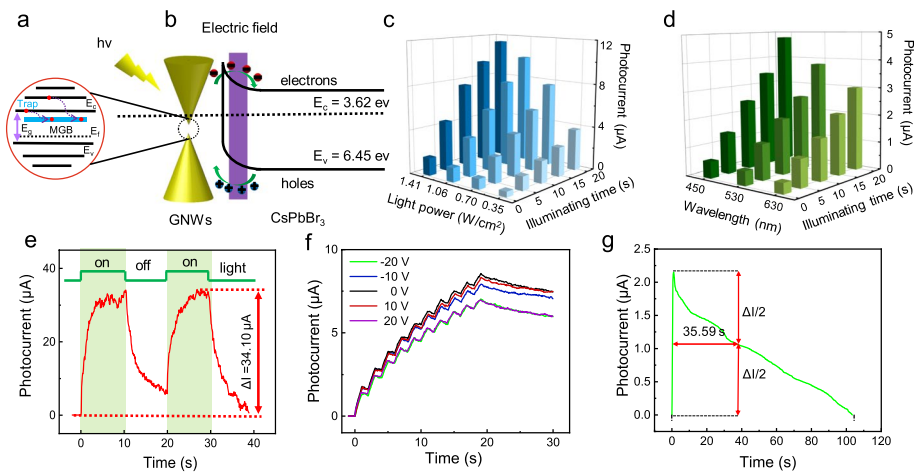


Fig. 3 Photoresponsive characteristics of GNWs/CsPbBr₃ QDs artificial optoelectronic synapses. **a** Schematic of middle energy bands of GNW. **b** Schematic of the energy bands of GNWs/CsPbBr₃ QDs heterostructure. **c** The photocurrent values of the synapses stimulated by a 530 nm laser pulse at different power and exposure durations. **d** The photocurrent values of the synapses stimulated by a power density 0.35 W/cm² laser pulse at different wavelengths and exposure times. **e** Time-dependent photocurrent changes under power density 1.90 W/cm² 360 nm laser pulses. **f** The photocurrent changes of the synapses stimulated by a power density 1.90 W/cm² 530 nm laser pulse train at different gate voltages (Pulse width: 1 s, pulse interval: 1 s). **g** Photocurrent decay curve stimulated by a 530 nm laser pulse with the laser power of 1.90 W/cm² and the pulse width of 1 s

significant long-term response of the artificial optoelectronic synapses, and thus to realizing the perceptual learning function.

Laser response characteristics of the synaptic device

The natural defects of GNWs can form the middle energy band (MGB) electron capture center on the boundary and surface (Fig. 3a). For the graphene with certain defects, the band gap opens [49]. The MGB refers to the defect structure of graphene, which forms a unique bandgap between the conduction and the valence bands [16]. GNWs have proved to contain many defects from the high D peak of the Raman spectrum (Fig. 2d). The photocurrent recovery time in GNWs is significantly longer than that of high-quality graphene films [50]. In high-quality graphene, the lifetime of photogenerated carriers is typically only picoseconds [51]. Therefore, it can be concluded that the defects in GNWs lead to the trapping effect of photogenerated carriers, which extends the lifetime of photogenerated carriers. The defects of GNWs themselves will cause the photogenerated carriers to be trapped, resulting in the slow recovery of the photocurrent after the laser beam was turned off. The emergence of the middle energy band reduces the electron-phonon scattering rate from the conduction to the valence band. Therefore, more photogenerated electrons and secondary generated electrons can be captured in MGB, resulting in a longer lifetime of photogenerated carriers [52]. After doping CsPbBr₃ QDs, a heterostructure is formed between GNWs and CsPbBr₃ QDs. The corresponding energy band diagram is shown in Fig. 3b. The direction of the built-in electric field points from the CsPbBr₃ QDs to GNWs. When illuminated by a laser beam, photogenerated carriers are mainly generated in CsPbBr₃ QDs, and GNWs also absorb the laser to generate some photogenerated carriers. The built-in electric field separates

the photogenerated carriers so that the lifetime of the photogenerated carriers is further extended.

The photocurrent evolution of the HC-type optoelectronic synapses is measured. The photocurrent responses of the 530 nm laser pulse irradiation at different powers and exposure times are shown in Figs. 3c and S4. Prolonging the irradiation time and enhancing the laser power lead to an increase in the photocurrent intensity. This trend is not infinite, however, and the photocurrent tends to saturate after a period of illumination. A similar trend of the photocurrent changes is demonstrated under 630 nm and 450 nm laser pulse irradiation at different powers and exposure times (Fig. S5). The photocurrent response at different wavelengths is shown in Fig. 3d. The results under 0.35 W/cm^2 suggest that the lower wavelength can produce a stronger photocurrent, which is consistent with the changes induced by 0.70 W/cm^2 , 1.06 W/cm^2 , and 1.41 W/cm^2 laser beams (Fig. S6). In the future, to reduce power consumption, one of the pathways is to decrease the light power. Moreover, reducing the device area is also effective, because the energy consumption is proportional to the light absorption area of the synapse. Through high-precision lithography technologies such as e-beam and two-photon absorption lithography, the energy consumption of the device can be greatly reduced, which can also effectively realize the fabrication of the device array. In addition, we suggest that reducing the contact resistance between electrodes and GNWs by optimizing the device fabrication process can also decrease energy consumption.

An excellent synaptic optoelectronic characteristic is shown under irradiation of a laser source with a wavelength of 360 nm and a power of 1.90 W/cm^2 (Fig. 3e). Herein the pulsed laser beam was repeatedly irradiated for 10 s with a 10 s interval, leading to a photocurrent change as high as $34.1 \mu\text{A}$. The repeatability experiment was carried out at 1.90 W/cm^2 laser intensity, and the photocurrent intensity was maintained at 98.24 % at 400 s (Fig. S7). This indicates that under strong laser illumination, the CsPbBr₃ QDs degrade.

The device has significant voltage-modulated photoplasticity. As illustrated in Fig. 3f, the photocurrent changes can be suppressed by applying different gate voltages. Since the perovskite QDs are attached to the surface of the vertical-located GNWs, the electric field generated by the gate voltage (no matter whether upward or downward) weakens the interaction between QDs and n-type doped GNWs (Fig. S8). Consequently, the photocurrent response is reduced when the gate voltages are applied.

The GNWs/CsPbBr₃ QDs synapses exhibit significant long-term optoelectronic response. As shown in Fig. 3g, the half-life period of the photocurrent decay is 35.59 s after illumination by a 1.90 W/cm^2 laser pulse. Compared with the periods in reported devices (Table 1) [14, 20–34], the GNWs/CsPbBr₃ QDs synapses have both a long memory time and a microampere-level photocurrent, owing to the combined effect of the MGB and the built-in electric field formed at the GNWs/CsPbBr₃ QDs interface. A complete neuromorphic computing system requires the integration of the processor and many other electronic circuits. At this stage, electronic circuits typically work with microampere currents. Therefore, optoelectronic synapses that achieve microampere photocurrent responses can be integrated more effectively with other electronic circuits.

A controllable memory characteristic of the synapses is demonstrated through the paired-pulse facilitation (PPF) measurement. PPF refers to the enhanced postsynaptic

Table 1 Comparison between previous HC type optoelectronic synapses and this work

Synapse material	Half-life period	Photocurrent	Laser pulse stimulation time	Ref.
IGZO	2.7 s	0.71 nA	300 ms	[14]
PDVT-10/N2200	0.4 s	3 nA	50 ms	[20]
PbS QDs/Graphene	1 s	9 μ A	1.25 s	[21]
C8-BTBT/ITO	8 s	3.25 μ A	1 s	[22]
CsPbBr ₃ QDs/ PEDOT	25 s	30 nA	1 s	[23]
SnO ₂	0.1 s	482 nA	100 ms	[24]
Alkylated GO/IGZO	15.29 s	2.1 nA	50 ms	[25]
CsPbBr ₃ QDs/PMMA	41.237 s	11.3 nA	1 s	[26]
Artificial visual perception circuit	0.937 s	785.7 nA	500 ms	[27]
LOND	0.1 s	1.16 nA	120 ms	[28]
CsBi ₃ I ₉ /PDPP4T	2 s	1.25 nA	1 s	[29]
MAPbI ₃ /Si nanomembrane	5 s	2 nA	200 ms	[30]
CsPbBr ₃ /PEDOT	40 s	6.9 μ A	15 s	[31]
WS ₂	1.11 s	0.16 nA	100 ms	[32]
Pbs	23 s	23.8 nA	2s	[33]
MoS ₂	11.81 s	34.48 nA	10 ms	[34]
CsPbBr ₃ /GNWs	35.59 s	2.24 μ A	1 s	This work

response caused by two consecutive synaptic stimulations and exists in biological excitatory and inhibitory synapses. It plays a vital role in recognizing and decoding visual and auditory signals and other temporal-dependent information [53, 54]. Figure 4a and b show the photocurrent curves of the synapses stimulated by laser pulses at different wavelengths. Using A_1 to represent the photocurrent change stimulated by the first laser pulse, and A_2 to represent the change stimulated by the second laser pulse, the PPF index refers to the ratio of A_2/A_1 [55]. Figure 4c shows the relationship between the PPF index and the interval (Δt) of the two-laser pulses. The pulsed laser density is 1.90W/cm² and the pulse frequency is 1 Hz. It is found that the relationship between A_2/A_1 and Δt follows a double exponential function,

$$\text{PPF} = y_0 + C_1 * \exp(-\Delta t/t_1) + C_2 * \exp(-\Delta t/t_2) \quad (3)$$

where C_1 (C_2) and t_1 (t_2) are the initial facilitation degree and characteristic relaxation time of the decay term, respectively. t_1 of 0.24459 s and t_2 of 10.44171 s can be obtained by fitting. Obviously, t_2 is approximately one order of magnitude higher than t_1 , which is very consistent with the measurement data in biological synapses [56]. The photocurrent curves for the PPF measurement have been provided in Fig. S9. Moreover, the PPF behaviors also emerge on the synapses stimulated by 450 nm and 630 nm laser pulses (Fig. S10).

The memory duration of the GNWs/CsPbBr₃ QDs optoelectronic synapses can be controlled by the numbers and frequencies of laser pulses. Figure 4d and e show the photocurrent changes induced by different pulse numbers (1, 5, 20, and 50) or frequencies (0.1 Hz, 0.25 Hz, 0.5 Hz, and 1 Hz) of 530 nm laser pulses. When the pulse number and frequency increase, the photocurrent changes turn strong and the memory duration turns long. Pulsed laser stimulation at 450 nm and 630 nm also showed controllable

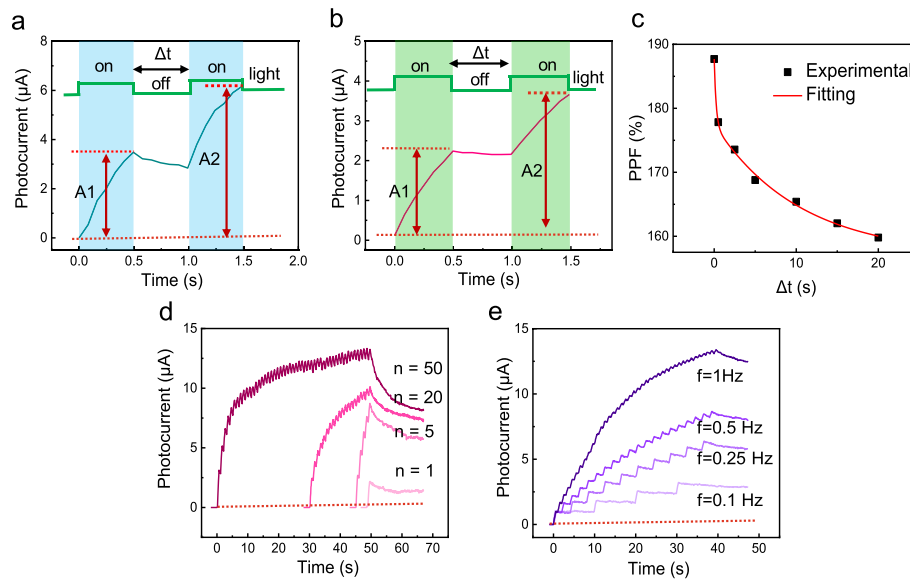


Fig. 4 Controllable photoresponsive characteristics of the GNWs/CsPbBr₃ QD artificial optoelectronic synapse under pulsed laser train stimuli. **a** The photocurrent response curve of the device illuminated by two 450 nm laser pulses (1.90 W/cm², pulse width: 0.5 s, pulse interval: 0.5 s). **b** The photocurrent response curve of the device illuminated by two 530 nm laser pulses (1.90 W/cm², pulse width: 0.5 s, pulse interval: 0.5 s). **c** The variation of paired-pulse facilitation index with the interval of laser pulse pairs. The pulse frequency is 1 Hz. **d, e** Controllable photocurrent response induced by increasing the pulse number and frequency of 1.90 W/cm² 530 nm pulsed laser stimulation

memory characteristics (Fig. S11), which are basic mechanisms of perceptual learning. An interesting phenomenon is that we found the photocurrent decays faster at 450 nm and 630 nm compared with the 530 nm laser. We suggest that it is because the photon energy at 530 nm wavelength is closer to the bandgap width of CsPbBr₃ QDs, so the built-in electric field prolongs the carrier lifetime more obviously.

Perceptual learning simulation

The GNWs/CsPbBr₃ QDs optoelectronic artificial synapse can mimic typical perceptual learning - an image recognition process of human retinal neuron networks. We measured the photocurrent of a GNWs/CsPbBr₃ QDs synapse was measured under different power densities and pulse numbers, and then simulated a 28×28 photocurrent array of the optical image of “8”, which was selected from the Mixed National Institute of Standards and Technology (MNIST) dataset [57]. Herein random noises were added to the MNIST image (Fig. S12). Figure 5a presents the image of the digital “8” pattern induced by 1, 5, 10, 15, and 20 laser pulses with a power of 0.35 W/cm². Under one laser pulse stimulation, the image resolution is poor owing to the influence of noise. With the increase in the pulse numbers, the signal-to-noise ratios gradually increase, and thus the images turn clear. After the laser pulses are applied, the further resolution change of the handwritten digit “8” can be considered a perceptual forgetting process. As shown in Fig. 5b, with the increase in the forgetting process duration, an image resolution decrease is demonstrated. This process is similar to the process of gradually forgetting after the brain remembers the image. Figure 5c shows the digital “8” images stimulated under various laser pulse powers. As the laser powers enhance the contrasts of the image

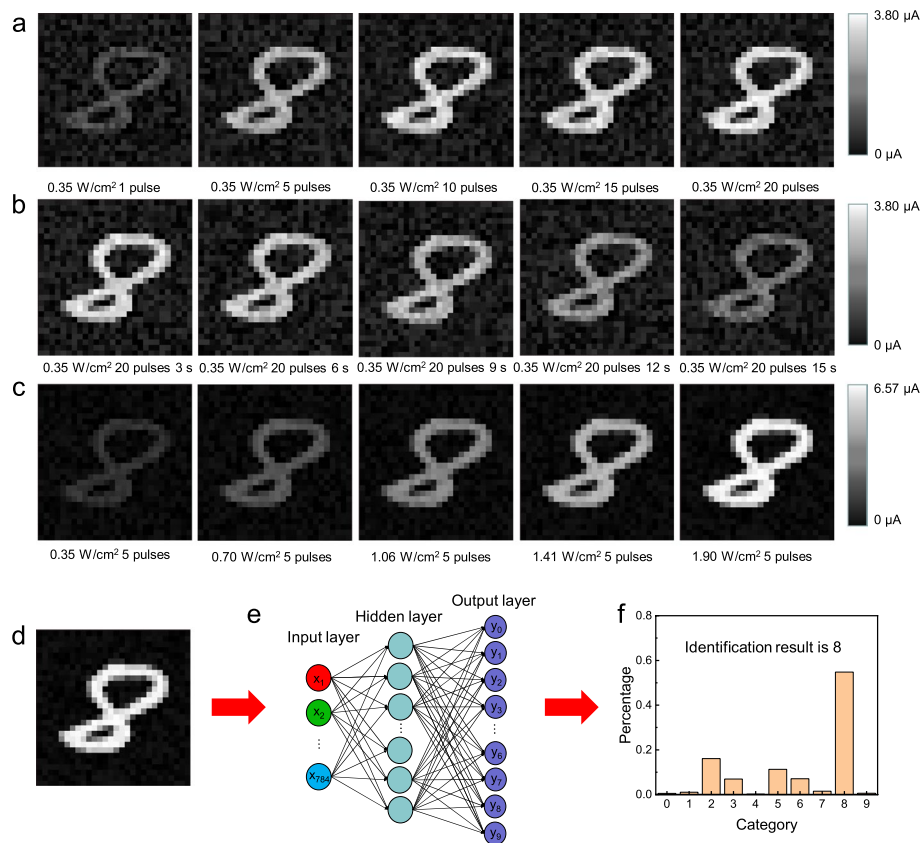


Fig. 5 The image recognition process using a GNWs/CsPbBr₃ QDs artificial optoelectronic synapse array. **a** Time-dependent grayscale images of handwritten digit “8” stimulated with different numbers of 530 nm laser pulses. **b** Time-dependent grayscale images of the “8” forgetting process after the stimulation with a train of 20 530 nm pulses. **c** Time-dependent grayscale images of “8” stimulated with five laser pulses at different powers. **d** Input the grayscale image of handwritten digit “8” with 28×28 pixels. **e** Image recognition process using an ANN. **f** Weight map simulated by the ANN

increase because of the high photocurrent (Fig. 3c), indicating that the synaptic weights can be controlled using different powers.

Next, to perform the perceptual learning with the MNIST handwritten digits, an ANN consisting of the 28×28 synaptic array and 10 output neurons was designed [58]. Figure 5d and e present the digital “8” grayscale image (28×28 pixels) and the ANN structure. The input is a 784-pixel image and the output neurons correspond to numbers 0-9. Figure 5f shows the image recognition result of 5 laser pulses. The percentage values of each category in the output neurons represent the probability of the corresponding number. Since the probability of the number 8 is the largest, the ANN successfully recognizes the handwritten digital image as the digital number “8.”

Through the ANN we have demonstrated that the ability of sensory systems to respond to stimuli can be enhanced through a learning experience, which is a typical characteristic of perceptual learning. Figure 6a shows the recognition accuracies of 10000 MNIST test images corresponding to different pulse numbers and pulse powers. The accuracies are improved considerably with the increase of the pulse numbers. The accuracy after 20 laser pulses with a power density of 1.9 W/cm^2 is 96.42 %, around 2.4 times higher than that after one pulse. Moreover, the laser power increase

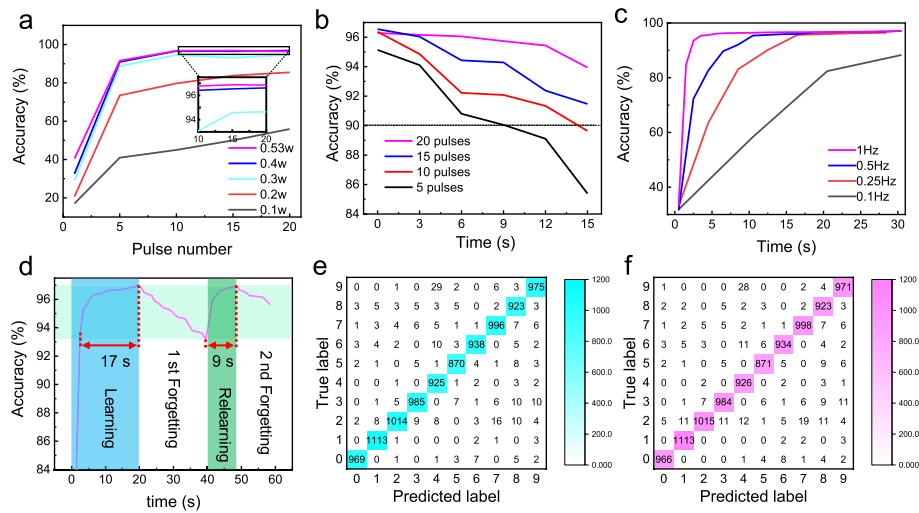


Fig. 6 Perceptual learning demonstration. **a** The influence of different laser pulse numbers and powers on the image recognition accuracies. The wavelength of the stimulation laser pulse is 530 nm. **b** Image recognition accuracies during the forgetting process. The synapses were stimulated with 530 nm laser pulses with different numbers. **c** The relationship between the accuracies and the laser pulses with different frequencies. **d** The accuracies change during the learning–forgetting–relearning process. The synapses were stimulated with 1.90 W/cm^2 530 nm laser pulses. **e** The confusion matrix of the test image after 17-second learning. The accuracy is 97.08 %. **f** The confusion matrix of the test image after 9-second relearning. The accuracy is 97.01 %

can also improve the image recognition accuracy, but when the power density is above 1.06 W/cm^2 , the accuracies gradually reach saturation. We also realized a property of controllable perceptual forgetting, based on the long-term photocurrent response of the synapse. After training processes in which 5, 10, 15, and 20 1.90 W/cm^2 laser pulses are applied, the recognition accuracies under various forgetting durations were simulated. As shown in Fig. 6b, even after a 15 s forgetting process, the recognition accuracies can be well maintained above 90 %.

Combining the controllable properties of perceptual learning and forgetting, we have achieved a strong and continuous ability of image recognition under a low learning frequency. Herein the relationship between the pulse frequencies (0.1 Hz, 0.25 Hz, 0.5 Hz, and 1 Hz) and the recognition accuracies was investigated (Fig. 6c). High frequencies lead to high accuracies within seconds, while under a frequency as low as 0.1 Hz, a strong image recognition ability with accuracies above 80 % emerges after a 30-second training.

Another typical characteristic of perceptual learning, in which less time is required to regain the lost ability that has been previously learned, has also been realized. The GNWs/CsPbBr₃ QDs synaptic array was excited by two laser pulse trains with a power density of 1.90 W/cm^2 and a frequency of 1 Hz successively. As shown in Fig. 6d, the image recognition accuracies enhance by the first pulse train. It takes 17 seconds to enhance the accuracies from 93% to 97%. The confusion matrix of the 97 % accuracy after the learning is shown in Fig. 6e. At the next step, the accuracies decline during the train interval, which mimics the phenomenon that the learned images tend to be gradually forgotten. After the accuracies decrease to the level of 93 %, the second pulse train launches the relearning process of image recognition. It only takes 9 seconds for the second pulse train to recover the accuracy loss (Fig. 6f). The interesting

“learning-forgetting-relearning” behavior verifies that the mimicking of human perceptual learning can be conducted by the synaptic array with a long-term photocurrent response.

Discussion

Human perceptual learning which forms complex cognitive processes can be maintained throughout life. The recognition accuracy of human sensory systems is time-dependent, and can be determined by how many and when the related learning process was performed. In this paper, we have verified that the high accuracy of image recognition can be retained even under a low-frequency learning process. In perceptual learning, the learning process can differentiate the input signal of useful objects among a lot of information, and turn it effective to be recognized. With the accumulation of the learning experience, the ability to differentiate the information is gradually improved. Moreover, due to the memorial effect from the synapses in the neuron network, the relearning process takes less time and energy consumption than those in the first learning. It is a basic mechanism for a human to quickly and effectively perceive information through visual, auditory, tactile, olfactory, and taste.

In summary, we reported a HC-type GNWs/CsPbBr₃ QDs optoelectronic synapse for the demonstration of human perceptual learning. The synapses can be controllably stimulated by visible laser pulses at different numbers, powers, wavelengths, and frequencies. Through the introduction of GNWs as the QD substrate, the synapse has a long photocurrent decay time owing to the introduction of the unique MGB of GNWs and the use of the built-in electric field between GNWs and CsPbBr₃ QDs. Pulsed laser stimulation at 530 nm for 1 s, the half-life period of the photocurrent decay is as high as 35.59 s. The laser response intensity of the transistor-type structure design can be flexibly adjusted by applying an external gate voltage, which can imitate the regulation of the brain's synaptic excitement in the biological system. Moreover, the laser response results of the device can be processed in a typical neuromorphic way, such as PPF and memory duration tuning. The GNWs/CsPbBr₃ QDs optoelectronic synapse can be combined with an ANN, to mimic a kind of human perceptual learning - handwritten digit recognition. Under twenty laser power training, the recognition accuracy is as high as 96.42 %. A rapid accuracy increase is achieved by increasing the numbers and powers of the laser pulses, which is a typical characteristic of perceptual learning. In addition, we have shown that the relearning process takes less time to gain an accuracy enhancement than the first learning. The realization of human perceptual learning has great potential for high-performance artificial intelligence sensory devices.

Materials and methods

Synapse fabrication

A heavily p-doped Si wafer with a 300 nm SiO₂ layer was rapidly heated to 910 °C at a rate of 200 °C/min and annealed for 5 min in an H₂ atmosphere with 500 sccm. During PECVD deposition of an GNW array, the pressure was controlled to be 5.5 mbar. 5 sccm CH₄, 16 sccm H₂, and 300 sccm Ar were introduced into the chamber. After waiting for 15 s, the plasma was turned on for 12 min with a power of 30 W and a frequency of 10

kHz. Next, the GNW array was patterned by oxygen plasma etching and photolithography. 15 nm Ti/300 nm Au layers were thermal-deposited. Finally, the CsPbBr₃ QDs, bought from Suzhou Xingshuo Nanotech Co. Ltd, were spin-coated on the GNWs.

Synapse material characterization

The TEM images were acquired on a Tecnai F20 TEM. SEM measurements were carried out on a ZEISS Gemini 300 microscope. The CsPbBr₃ QDs solution was diluted at 1:50 and then 10 microliters were dropped on the silica glass slide. The absorption spectrum was measured by ultraviolet spectrophotometry with a wavelength range from 300 nm to 800 nm. A fluorescence spectrometer (Edinburgh FLS1000) was used to measure the emission spectrum and carrier lifetime of the CsPbBr₃ QDs. The excitation wavelength was 450 nm during the experiment, and the monitoring wavelength was 530 nm. We used HORIBA Raman equipment to measure the Raman spectra of GNWs. The laser wavelength selected was 530 nm.

Synapse characterization

All the electrical measurements were conducted with a precision semiconductor parameter analyzer (4200 SCS, Keithley) under a 4 V bias. The laser pulses were generated on a fiber-optic laser controlled by a signal generator. Figure S13 shows that the photocurrent curves in Figs. 3 and 4 were obtained by subtracting the dark current from the total current. Each group of experiment results was measured three times and taken with the average value. During the gate voltage measurement, a 4 V source-drain bias was used. We used 5 laser powers in our measurement (0.1 W, 0.2 W, 0.3 W, 0.4 W and 0.53 W), and the corresponding power densities are 0.35 W/cm², 0.70 W/cm², 1.06 W/cm², and 1.41 W/cm² and 1.90 W/cm².

ANN design and image recognition simulation

Twenty thousand training images and 10,000 test images of handwritten digits from 0 to 9, with 28 × 28 pixels, were selected from the MNIST dataset. Random noises were added to these images. The ANN contains 784 input neurons and 10 output neurons. The photocurrent of a GNWs/CsPbBr₃ QDs synapse was measured under different power densities and pulse numbers. We defined the photocurrent under the illumination of a 1.9 W/cm² beam with 20 pulses as the pixel grayscale value of 255. Next, a direct proportion relationship between the grayscale value and the photocurrent was set to obtain the photocurrent maps for image recognition. The simulation algorithm was developed by the Python language, in which the synaptic weights were updated by the stochastic gradient ascent/descent algorithm. The learning rate was determined to be 0.01, and the expected error value was set as 1 × 10⁻³. Each output neuron produced a signal from 0 to 1 using a sigmoid function.

Abbreviations

HC	Heterostructure channel
GNWs	Graphene nanowalls
QDs	Quantum dots
ANN	Artificial neuron network
PECVD	Plasma-enhanced chemical vapor deposition
TEM	Transmission electron microscopy

HRTEM	High-resolution transmission electron microscopy
PL	Photoluminescence
MGB	Middle energy band
PPF	Paired-pulse facilitation
MNIST	Mixed National Institute of Standards and Technology

Supplementary Information

The online version contains supplementary material available at <https://doi.org/10.1186/s43074-023-00082-8>.

Additional file 1: Fig. S1. The fabrication flowchart and optical images of a photoelectric synapse array based on GNWs and CsPbBr₃ QDs. **Fig. S2.** SEM images of the top-view GNWs. **Fig. S3.** An absorption spectrum of the CsPbBr₃ QDs. **Fig. S4.** Basic photoresponsive characteristics of the GNWs/CsPbBr₃ QDs optoelectronic synapse. **Fig. S5.** The photocurrent values of the synapses under different laser pulse powers and illuminating times. **Fig. S6.** Effects of different wavelengths and irradiation times on the photocurrent response. **Fig. S7.** Comparison of photocurrent intensity before and after 400 s illumination. **Fig. S8.** Transfer characteristic curve of the device. **Fig. S9.** The measurement results of the PPF property of the device with different laser pulse intervals. **Fig. S10.** The PPF effect of the synapse stimulated by laser pulses with different wavelengths. **Fig. S11.** The photocurrent of the device stimulated by 450 (a) and 630 (b) nm laser pulse trains under different pulse numbers. **Fig. S12.** Handwritten digital image processing for recognition simulation. **Fig. S13.** Total current measured under the laser density of 1.90 W/cm².

Acknowledgements

We would like to thank the Artificial-Intelligence Nanophotonics, School of Optical-Electrical and Computer Engineering, University of Shanghai for Science and Technology and Key Laboratory of Optoelectronic Technology, Beijing University of Technology Centre for supporting this work.

Authors' contributions

Min Gu, Xi Chen, Yibo Dong, and Zengji Yue conceived the idea. Runze Li and Yibo Dong contributed equally to this work. Zengji Yue and Xi Chen designed and supervised the experiments. Runze Li and Yibo Dong conducted the experiments, analyzed the data, and drafted the manuscript. All authors contributed to the paper's writing and discussion. The author(s) read and approved the final manuscript.

Funding

This research was supported by the Shanghai Municipal Science and Technology Major Project, the Science and Technology Commission of Shanghai Municipality (STCSM) with No. 21DZ1100500, the Zhangjiang National Innovation Demonstration Zone (ZJ2019-ZD-005), National Natural Science Foundation of China (11974247), and China Postdoctoral Science Foundation (2021M692136).

Availability of data and materials

GNWs were obtained from Key Laboratory of Optoelectronic Technology, Beijing University of Technology. The CsPbBr₃ QDs were purchased from Suzhou Xingshuo Nanotech Co. Ltd.

Declarations

Ethics approval and consent to participate

Not applicable.

Consent for publication

Not applicable.

Competing interests

The authors declare that they have no competing interest.

Received: 29 September 2022 Revised: 11 December 2022 Accepted: 2 January 2023

Published online: 11 January 2023

References

- Dai S, Zhao Y, Wang Y, Zhang J, Fang L, Jin S, et al. Recent advances in transistor-based artificial synapses. *Adv Funct Mater.* 2019;29(42):1903700.
- Emboras A, Alabastri A, Lehmann P, Portner K, Weilenmann C, Ma P, et al. Opto-electronic memristors: Prospects and challenges in neuromorphic computing. *Appl Phys Lett.* 2020;117(23):230502.
- Xiao Z, Huang J. Energy-efficient hybrid perovskite memristors and synaptic devices. *Adv Electron Mater.* 2016;2(7):1600100.
- Zhai Y, Yang J-Q, Zhou Y, Mao J-Y, Ren Y, Roy VAL, et al. Toward non-volatile photonic memory: concept, material and design. *Mater Horiz.* 2018;5(4):641–54.
- Watanabe T, Nández JE, Sasaki Y. Perceptual learning without perception. *Nature.* 2001;413(25):844–8.
- Chen Z, Yu Y, Jin L, Li Y, Li Q, Li T, et al. Artificial synapses with photoelectric plasticity and memory behaviors based on charge trapping memristive system. *Mater Design.* 2020;2020(188):108415.

7. Emboras A, Goykhman I, Desiatov B, Mazurski N, Stern L, Shappir J, et al. Nanoscale plasmonic memristor with optical readout functionality. *Nano Lett.* 2013;13(12):6151–5.
8. Shulaker MM, Hills G, Park RS, Howe RT, Saraswat K, Wong HP, et al. Three-dimensional integration of nanotechnologies for computing and data storage on a single chip. *Nature.* 2017;547(7661):74–8.
9. Kim K, Chen CL, Truong Q, Shen AM, Chen Y. A carbon nanotube synapse with dynamic logic and learning. *Adv Mater.* 2013;25(12):1693–8.
10. Wang X, Shao Q, Ku PS, Ruotolo A. A memristive diode for neuromorphic computing. *Microelectron Eng.* 2015;2015(138):7–11.
11. Lee TH, Loke D, Huang KJ, Wang WJ, Elliott SR. Tailoring transient-amorphous states: towards fast and power-efficient phase-change memory and neuromorphic computing. *Adv Mater.* 2014;26(44):7493–8.
12. Kim S, Du C, Sheridan P, Ma W, Choi S, Lu WD. Experimental demonstration of a second-order memristor and its ability to biorealistically implement synaptic plasticity. *Nano Lett.* 2015;15(3):2203–11.
13. Tan ZH, Yang R, Terabe K, Yin XB, Zhang XD, Guo X. Synaptic metaplasticity realized in oxide memristive devices. *Adv Mater.* 2016;28(2):377–84.
14. Lee M, Lee W, Choi S, Jo JW, Kim J, Park SK, et al. Brain-inspired photonic neuromorphic devices using photodynamic amorphous oxide semiconductors and their persistent photoconductivity. *Adv Mater.* 2017;29(28):1700951.
15. Zhu X, Lu WD. Optogenetics-inspired tunable synaptic functions in memristors. *ACS Nano.* 2018;12(2):1242–9.
16. Zhang BY, Liu T, Meng B, Li X, Liang G, Hu X, et al. Broadband high photoresponse from pure monolayer graphene photodetector. *Nat Commun.* 2013;2013(4):1811.
17. Zhang Q, Yu H, Barbiero M, Wang B, Gu M. Artificial neural networks enabled by nanophotonics. *Light Sci Appl.* 2019;2019(8):42.
18. Wang G, Wang R, Kong W, Zhang J. Simulation of retinal ganglion cell response using fast independent component analysis. *Cogn Neurodyn.* 2018;12(6):615–24.
19. Sabesan R, Schmidt BP, Tuten WS, Roorda A. The elementary representation of spatial and color vision in the human retina. *Neuroscience.* 2016;2(9):e1600797.
20. Gao C, Yang H, Li E, Yan Y, He L, Chen H, et al. Heterostructured vertical organic transistor for high-performance optoelectronic memory and artificial synapse. *ACS Photonics.* 2021;8(10):3094–103.
21. Sun Z, Liu Z, Li J, Tai GA, Lau SP, Yan F. Infrared photodetectors based on CVD-grown graphene and PbS quantum dots with ultrahigh responsivity. *Adv Mater.* 2012;24(43):5878–83.
22. Fang L, Dai S, Zhao Y, Liu D, Huang J. Light-stimulated artificial synapses based on 2D organic field-effect transistors. *Adv Electron Mater.* 2019;6(1):1901217.
23. Chen T, Wang X, Hao D, Dai S, Ou Q, Zhang J, et al. Photonic synapses with ultra-low energy consumption based on vertical organic field-effect transistors. *Adv Opt Mater.* 2021;9(8):2002030.
24. Chen Y, Qiu W, Wang X, Liu W, Wang J, Dai G, et al. Solar-blind SnO₂ nanowire photo-synapses for associative learning and coincidence detection. *Nano Energy.* 2019;2019(62):393–400.
25. Sun J, Oh S, Choi Y, Seo S, Oh MJ, Lee M, et al. Optoelectronic synapse based on IGZO-alkylated graphene oxide hybrid structure. *Adv Funct Mater.* 2018;28(47):1804397.
26. Wang Y, Lv Z, Chen J, Wang Z, Zhou Y, Zhou L, et al. Photonic synapses based on inorganic perovskite quantum dots for neuromorphic computing. *Adv Mater.* 2018;30(38):1802883.
27. Kwon SM, Cho SW, Kim M, Heo JS, Kim YH, Park SK. Environment-adaptable artificial visual perception behaviors using a light-adjustable optoelectronic neuromorphic device array. *Adv Mater.* 2019;31(52):1906433.
28. Wang H, Zhao Q, Ni Z, Li Q, Liu H, Yang Y, et al. A ferroelectric/electrochemical modulated organic synapse for ultraflexible, artificial visual-perception system. *Adv Mater.* 2018;30(46):1803961.
29. Wang R, Chen P, Hao D, Zhang J, Shi Q, Liu D, et al. Artificial synapses based on lead-free perovskite floating-gate organic field-effect transistors for supervised and unsupervised learning. *ACS Appl Mater Interfaces.* 2021;13(36):43144–54.
30. Yin L, Huang W, Xiao R, Peng W, Zhu Y, Zhang Y, et al. Optically stimulated synaptic devices based on the hybrid structure of silicon nanomembrane and perovskite. *Nano Lett.* 2020;20(5):3378–87.
31. Ma F, Zhu Y, Xu Z, Liu Y, Zheng X, Ju S, et al. Optoelectronic perovskite synapses for neuromorphic computing. *Adv Funct Mater.* 2020;30(11):1908901.
32. Luo ZD, Xia X, Yang MM, Wilson NR, Gruverman A, Alexe M. Artificial optoelectronic synapses based on ferroelectric field-effect enabled 2D transition metal dichalcogenide memristive transistors. *ACS Nano.* 2020;14(1):746–54.
33. Li H, Jiang X, Ye W, Zhang H, Zhou L, Zhang F, et al. Fully photon modulated heterostructure for neuromorphic computing. *Nano Energy.* 2019;65(2211):104000.
34. Zhang M, Fan Z, Jiang X, Zhu H, Chen L, Xia Y, et al. MoS₂-based Charge-trapping synaptic device with electrical and optical modulated conductance. *Nanophotonics.* 2020;9(8):2475–86.
35. Wang Y, Lv Z, Zhou L, Chen X, Chen J, Zhou Y, et al. Emerging perovskite materials for high density data storage and artificial synapses. *J Mater Chem C.* 2018;6(7):1600–17.
36. Cho SW, Kwon SM, Kim YH, Park SK. Recent progress in transistor-based optoelectronic synapses: from neuromorphic computing to artificial sensory system. *Adv Intell Syst.* 2021;3(6):2000162.
37. Dong Y, Gu Y, Zou Y, Song J, Xu L, Li J, et al. Improving all-inorganic perovskite photodetectors by preferred orientation and plasmonic effect. *Small.* 2016;12(40):5622–32.
38. Walsh A. Principles of chemical bonding and band gap engineering in hybrid organic-inorganic halide perovskites. *J Phys Chem C.* 2015;119(11):5755–60.
39. Xie C, Liu CK, Loi HL, Yan F. Perovskite-based phototransistors and hybrid photodetectors. *Adv Funct Mater.* 2019;30(20):1903907.
40. Mao JY, Zhou L, Zhu X, Zhou Y, Han ST. Photonic memristor for future computing: a perspective. *Adv Opt Mater.* 2019;7(22):1900766.
41. Kuzum D, Yu S, Wong HS. Synaptic electronics: materials, devices and applications. *Nanotechnology.* 2013;24(38):382001.

42. van de Burgt Y, Lubberman E, Fuller EJ, Keene ST, Faria GC, Agarwal S, et al. A non-volatile organic electrochemical device as a low-voltage artificial synapse for neuromorphic computing. *Nat Mater*. 2017;16(4):414–8.
43. Abbott LF, Regehr WG. Synaptic computation. *Nature*. 2004;431(7010):796–803.
44. Wang ZQ, Xu HY, Li XH, Yu H, Liu YC, Zhu XJ. Synaptic learning and memory functions achieved using oxygen ion migration/diffusion in an amorphous InGaZnO memristor. *Adv Funct Mater*. 2012;22(13):2759–65.
45. Sahoo B, Joseph J, Sharma A, Paul J. Surface modification of aluminium by graphene impregnation. *Mater Design*. 2017;2017(116):51–64.
46. Song JC, Rudner MS, Marcus CM, Levitov LS. Hot carrier transport and photocurrent response in graphene. *Nano Lett*. 2011;11(11):4688–92.
47. Sun D, Aivazian G, Jones AM, Ross JS, Yao W, Cobden D, et al. Ultrafast hot-carrier-dominated photocurrent in graphene. *Nat Nanotechnol*. 2012;7(2):114–8.
48. Seo HK, Kim H, Lee J, Park MH, Jeong SH, Kim YH, et al. Efficient flexible organic/inorganic hybrid perovskite light-emitting diodes based on graphene anode. *Adv Mater*. 2017;29(12):1605587.
49. Xu X, Liu C, Sun Z, Cao T, Zhang Z, Wang E, et al. Interfacial engineering in graphene bandgap. *Chem Soc Rev*. 2018;47(9):3059–99.
50. Qian F, Deng J, Xiong F, Dong Y, Hu L, Pan G, et al. Direct growth of high quality graphene nanowalls on dielectric surfaces by plasma-enhanced chemical vapor deposition for photo detection. *Opt Mater Express*. 2020;10(11):2909–18.
51. Tielrooij KJ, Piatkowski L, Massicotte M. Generation of photovoltage in graphene on a femtosecond timescale through efficient carrier heating. *Nat Nanotechnol*. 2015;2015(10):437–43.
52. Zhou D, Yu L, Zhu P, Zhao H, Feng S, Shen J. Lateral structured phototransistor based on mesoscopic graphene/perovskite heterojunctions. *Nanomaterials (Basel)*. 2021;11(3):641.
53. Hu SG, Liu Y, Chen TP, Liu Z, Yu Q, Deng LJ, et al. Emulating the paired-pulse facilitation of a biological synapse with a NiO_x-based memristor. *Appl Phys Lett*. 2013;102(18):183510.
54. Liu G, Wang C, Zhang W, Pan L, Zhang C, Yang X, et al. Organic biomimicking memristor for information storage and processing applications. *Adv Electron Mater*. 2016;2(2):1500298.
55. Gao S, Liu G, Yang H, Hu C, Chen Q, Gong G, et al. An oxide schottky junction artificial optoelectronic synapse. *ACS Nano*. 2019;13(2):2634–42.
56. Li HK, Chen TP, Liu P, Hu SG, Liu Y, Zhang Q, et al. A light-stimulated synaptic transistor with synaptic plasticity and memory functions based on InGaZnO_x-Al₂O₃ thin film structure. *J Appl Phys*. 2016;119(24):244505.
57. Lecun Y, Bottou L, Bengio Y, Haffner P. Gradient-based learning applied to document recognition. *P IEEE*. 1998;86(11):2278–324.
58. Zhu QB, Li B, Yang DD, Liu C, Feng S, Chen ML, et al. A flexible ultrasensitive optoelectronic sensor array for neuro-morphic vision systems. *Nat Commun*. 2021;12(1):1798.

Publisher's Note

Springer Nature remains neutral with regard to jurisdictional claims in published maps and institutional affiliations.

Submit your manuscript to a SpringerOpen[®] journal and benefit from:

- Convenient online submission
- Rigorous peer review
- Open access: articles freely available online
- High visibility within the field
- Retaining the copyright to your article

Submit your next manuscript at ► [springeropen.com](https://www.springeropen.com)
